Vision Research xxx (2016) xxx–xxx

Contents lists available at ScienceDirect

Vision Research

journal homepage: www.elsevier.com/locate/visres

The organization of the cone photoreceptor mosaic measured in the living human retina

Lucie Sawides *, Alberto de Castro, Stephen A. Burns

School of Optometry, Indiana University, 800E. Atwater Av., Bloomington, IN 47405, United States

ARTICLE INFO

Article history:
Received 15 March 2016
Received in revised form 15 June 2016
Accepted 22 June 2016
Available online xxxx

Keywords:
Adaptive optics imaging
Average cone photoreceptor
Anisotropy
Hexagonal packing
Organization
Clustering

ABSTRACT

The cone photoreceptors represent the initial fundamental sampling step in the acquisition of visual information. While recent advances in adaptive optics have provided increasingly precise estimates of the packing density and spacing of the cone photoreceptors in the living human retina, little is known about the local cone geometric arrangement beyond a tendency towards hexagonal packing. We analyzed the cone mosaic in data from 10 normal subjects. A technique was applied to calculate the local average cone mosaic structure which allowed us to determine the hexagonality, spacing and orientation of local regions. Using cone spacing estimates, we find the expected decrease in cone density with retinal eccentricity and higher densities along the horizontal as opposed to the vertical meridians. Orientation analysis reveals an asymmetry in the local cone spacing of the hexagonal packing, with cones having a larger local spacing along the horizontal direction. This horizontal/vertical asymmetry is altered at eccentricities larger than 2 degrees in the superior meridian and 2.5 degrees in the inferior meridian. Analysis of hexagon orientations in the central 1.4° of the retina shows a tendency for orientation to be locally coherent, with orientation patches consisting of between 35 and 240 cones.

1. Introduction

Studying the structural properties of the normal cone photoreceptor mosaic is important both to evaluate how the human visual system samples the world as well as to provide comparison date for understanding how aging and retinal diseases impact the sampling properties of the cone photoreceptors. The seminal paper by Curcio and colleagues (1990) expanded on earlier studies (Ahnelt, Kolb, & Pflug, 1987; Osterberg, 1935) to provide quantitative measures of the distribution and organization of the cone photoreceptors in post-mortem human retinae. It is now well accepted that for a given retinal eccentricity the cone density is higher along the horizontal (nasal and temporal) meridians than along the vertical (superior and inferior) meridians. Curcio and colleagues also computed local anisotropies in one eye (Curcio & Sloan, 1992) where they found that human cones are 10–15% farther apart along radii extending from the fovea than along isoeccentricity lines, (except at the edge of the rod-free zone, around 1° of retinal eccentricity).

Since that time, a number of approaches have been developed to make some of these measurements *in vivo*, including psychophysical experiments, based on interferometry (Coletta & Williams, 1987; Williams, 1988; Williams & Coletta, 1987) or speckle ocular interferometry (Marcos, Navarro, & Artal, 1996; Marcos, Tornow, Elsner, & Navarro, 1997) and scattering theory (Marcos & Burns, 1999). Most notable was the development of Adaptive Optics (AO) retinal imaging (Liang, Williams, & Miller, 1997), which allowed direct imaging of the cone mosaic in the living human retina. Using adaptive optics, it has been possible to individually identify cone photoreceptors and to quantify cone spatial organization (Chiu et al., 2013; Chui, Song, & Burns, 2008a, 2008b; Garrioch et al., 2012; Li & Roorda, 2007; Lombardo, Lombardo et al., 2013; Lombardo, Serrao, Ducoli, & Lombardo, 2013; Loquin et al., 2012; Merino, Duncan, Tiruveedhula, & Roorda, 2011; Roorda et al., 2002; Rossi & Roorda, 2010; Song, Chui, Zhong, Elsner, & Burns, 2011; Xue, Choi, Doble, & Werner, 2007; Zhang et al., 2015). A striking feature of quantitative photoreceptor data is the variability between and within individuals with a specific example being the variation in density of cones at the fovea. However, even at other fixed retinal locations, individuals vary widely in their photoreceptor packing density. While some studies reported the individual variability in cone packing between subjects (Li, Tiruveedhula, & Roorda, 2010; Song et al., 2011) other have described the variability in cone density within a subject at different retinal locations and

* Corresponding author.
E-mail address: lsawides@indiana.edu (L. Sawides).

http://dx.doi.org/10.1016/j.visres.2016.06.006
0042-6989/

eccentricities as well as global and local anisotropies in the cone photoreceptor packing within subjects (Chui et al., 2008a, 2008b).

The presence of anisotropies in the cone mosaic has been primarily studied using Voronoi diagrams (Shapiro, Schein, & De Monasterio, 1985). The Voronoi diagram, by connecting surrounding cones and characterizing the number of sides, allows assessment of the degree of hexagonality and how disease and aging can affect this aspect of packing geometry (Baraas et al., 2007; Carroll et al., 2009; Choi et al., 2006; Dees, Dubra, & Baraas, 2011; Lombardo, Serrao et al., 2013; Park, Chung, Greenstein, Tsang, & Chang, 2013). For Voronoi analysis to work well requires identifying every cone photoreceptor and positioning the center of each individual cone. Other methods, based on spatial frequency content, such as autocorrelograms (Rodieck, 1991) and the power spectrum of Fourier transform (Yellott, 1982), do not require the identification of each individual cone to quantify cone spacing and cones density. These studies have provided information on the hexagonality and spacing, but little information on local anisotropies of hexagonal packing. The presence of local anisotropies has been demonstrated in both human and non-human primate post-mortem tissue and the results suggest that cones tend to be clustered into relatively small regions of similar orientation (Ahnelt, 1998; Pum, Ahnelt, & Grasl, 1990).

In the current paper we introduce a technique, similar to the autocorrelation technique, which allows us to evaluate the cone mosaic on both a local and global basis. The new technique is based on cone-averaging to: (1) rapidly estimate cone spacing properties of the normal cone photoreceptor mosaic within relatively small areas without the need to identify every single cone (Burns, Zou, Qi, Zhong, & Huang, 2011); (2) evaluate the local anisotropy of the in-vivo cone photoreceptors mosaic, in the fovea as well as in the parafovea (up to 5° retinal eccentricity); and (3) provide estimates of the spatial organization and orientation mapping of the living human retina, similar to the analysis of Pum et al. (1990).

2. Materials and methods

2.1. Subjects

The right eye of each of 10 normal healthy subjects (ages of 24 to 36 years, mean 29.1 ± 3.6 yo) was imaged in the study. The average refractive error for the measured eyes was −1.55 ± 1.43 D (range 0 to −3.5D). Each subject's pupil was dilated with one drop of 0.5% tropicamide. The axial eye length for each subject was measured with a biometer (IOL Master; Carl Zeiss Meditec, Dublin, CA). Consent forms were obtained after a full explanation of the procedures and consequences of this study. The study protocol was approved by Indiana University Institutional Review Board and complied with the requirements of the Declaration of Helsinki.

2.2. High resolution adaptive optics scanning laser ophthalmoscope

We used the Indiana high resolution Adaptive Optics Scanning Laser Ophthalmoscope (AOSLO) (Burns et al., 2014; Ferguson et al., 2010). In brief, the system uses a supercontinuum laser source (Fianium Ltd., Southampton, UK) to provide both the wavefront sensing (856 nm; 50 μW at the cornea) and the infrared imaging source (810 nm; 200 μW at the cornea), a Shack-Hartmann wavefront sensor and a woofer-tweeter wavefront control system (Zou, Qi, & Burns, 2008) to provide en-face high-resolution images of retinal structures, with the capability of focusing on superficial or deeper retinal layers. Images were obtained at a 28 Hz frame rate and a 15.1 kHz line rate. Light returning from the retina passes through a confocal aperture optically conjugated to the retinal plane. In the current study, the system was focused on the cone photoreceptor layer. Depending on the retinal location of the cone photoreceptors imaged, we used three different computer controlled field sizes to measure cone spacing at different eccentricities: 1° × 0.9° imaging field (size 1: 0.5 μm/pixel sampling) for eccentricities up to 0.86°, a 1.3° × 1.2° imaging field (size 2: 0.67 μm/pixel sampling) for eccentricities from 0.90° to 1.28°and a 2° × 1.8° imaging field (size 3: 1 μm/pixel sampling) for eccentricities from 1.38° to 5.15°. We used a 25 μm confocal aperture (0.5 Airy disk confocal aperture) when imaging with size 1 and a 75 μm confocal aperture (1.5 Airy disk confocal aperture) when imaging with sizes 2 and 3. The subject's head movements were stabilized using a chin and forehead rest.

2.3. Imaging the cone photoreceptors in the fovea and parafovea

Measurements of foveal cones in the center of the fovea were recorded while the subjects fixated at 9 locations of the 1° × 0.9° (size1) imaging field (4 corners, 4 middle edges and the center). Thus, nine retinal images were obtained comprising a ~2 × 2° montage of foveal cones with a 0.5 μm/pixel sampling size. A strip along the superior or inferior meridian – until finding a blood vessel (approximately 1° × 3° strip) – was also imaged by steering the imaging beam while the subject maintained fixation on a fixed central target provided by an auxiliary fixation system. This additional strip of images was used to improve alignment of montages derived from the same retinal location but with different sampling.

To image the parafoveal cones, four strips of cones along the four primary meridians (Temporal (T), Nasal (N), Superior (S), Inferior (I)) were recorded by steering the 2° × 1.8° (size 3) imaging field in a 1° step from the fovea to the parafovea up to 5° retinal eccentricity while maintaining fixation on the central fixation target. To ensure alignment between field sizes we repeated the measurement of foveal cones across the center of the fovea with the size 3 imaging field (subjects pointing their eyes at 9 locations of the imaging field as described for the small field size).

Additionally, 4 subjects (S2, S5, S7 and S8) were imaged by steering the 1.3° × 1.2° (size 2) imaging beam around the fovea in order to compute accurately the cone spacing and cone density at eccentricities from 0.90° to 1.28° along the four meridians. The measurements on S2, S5 and S8 were performed without dilation of the pupil as they had a pupil size larger than 6 mm. These measurements were performed in a different session on a different day – one to two months after the initial measurements.

The whole procedure for AOSLO imaging on each subject took less than 30 min.

2.4. Image processing and montaging with automated custom software

Images of cones were recorded as short videos (100 frames at 580 × 520 pixel/frame) digitized at each retinal location for later processing which involves the correction of scan distortion, an automatic selection of a template image from each video segment, and the alignment of the remaining frames at that location to the template frame. The result was a series of short video sequences with eye movement removed. We then generated averages based on the local best contrast (Huang, Zhong, Zou, & Burns, 2011) for each retinal location.

Images from different retinal locations were next automatically aligned to create continuous montages with a custom MATLAB routine that combined MATLAB (Mathworks, Natick MA), i2 k Retina (DualAlign, LLC) (using the command line executable of i2k Retina) and Photoshop (Adobe Photoshop CS6 extended) using the Photoshop MATLAB toolbox.

Please cite this article in press as: Sawides, L., et al. The organization of the cone photoreceptor mosaic measured in the living human retina. *Vision Research* (2016), http://dx.doi.org/10.1016/j.visres.2016.06.006

2.5. Locating the foveal center as the peak of highest cone density

We used the foveal center, defined as the point of highest cone density as an origin for our spatial measurements. We first calculated the cone density over the 2° × 2° foveal montage with an automated custom MATLAB-based program that automatically identified individual cones and then calculated the density with a sampling window of 50 μm. We fitted the density data to a Gaussian function using MATLAB function fminsearch (with the free parameters being the coordinates of the center of the Gaussian, the sigma values and the amplitude), and we defined the fovea as the center of the best-fitting Gaussian. To deal with points that are outliers (low-quality average-cone image in a specific location giving an inaccurate cone density) we removed points with the highest deviation from the fitting, and then refit and obtained the center of the Gaussian density distribution, and used this as an origin for other measures. This fitting routine was used only to provide an origin for the coordinate system for the remainder of the analysis.

2.6. Analysis

Variations in individual retinal magnification were corrected based on measured axial lengths (Chui et al., 2008a, 2008b). The structural properties of the cone mosaic within local regions were computed using a custom program written in MATLAB, which automatically identified individual cones with a method similar to that of Li and Roorda (2007). To automatically detect cones in the fovea as well as in the parafovea we used three different sizes of spatial filters ranging from small, for foveal data, to large, for parafoveal data. Because our analysis does not require detecting every cone we tuned our algorithm to have slightly decreased sensitivity and a corresponding decrease in false positives. Thus, while similar, this routine had some differences from the Li and Roorda algorithm. We did this by accepting detected cones based on their brightness relative to the mean of the local analysis window, excluding dim detections (cones that had a brightness less than 1.2 standard deviations (SD) below the mean brightness) as well as cones that were very bright (more than 3SD greater than the mean).

To perform the cone counting analysis, we used a sliding 50 × 50 pixel window within 3° of the fovea and a sliding 100 × 100 pixel window for eccentricities larger than 3.0° which correspond to a 25 × 25 μm (retinal eccentricity <0.9°), a 34 × 34 μm (from 0.90° to 1.28° retinal eccentricity), a 50 × 50 μm (from 1.38° to 3° retinal eccentricity) or a 100 × 100 μm (retinal eccentricity >3°) window. Within the sliding window, we then located cones in a centered region one half the size of the sliding window (corresponding to centered 12.5 × 12.5 μm (retinal eccentricity <0.9°), 17 × 17 μm (from 0.90° to 1.28° retinal eccentricity), 25 × 25 μm (from 1.38° to 3° retinal eccentricity) or 50 × 50 μm (retinal eccentricities larger than 3.0°) regions. The analysis regions were spaced at either 25 or 50 pixels such that no cone was used in more than one analysis window.

Building an average-cone image. For each region, cones detected by the routine were extracted, together with a surrounding area of 25 × 25 pixels (12.5 μm × 12.5 μm in the fovea and 25 × 25 μm in the parafovea) centered on the detected cone. These individual images were then rescaled to increase their size 6 times (using MATLAB function imresize), thus oversampling and decreasing the pixel size. This produced for each region a series of images, each with a cone at the center. We then averaged these images to calculate an "average-cone image". The average cone images generated a series of estimates of the local surround of the cones in each retinal location. These typically appear as a hexagonally arranged blobs, (Figs. 1 and 2) since the fine details of the cones are smoothed by the averaging. These average images were used for analysis in the rest of the manuscript.

Average cone spacing. From each average-cone image, we measured the average cone spacing by computing a radial profile and finding the first maximum. From the spacing the cone density was calculated assuming hexagonal packing. The average cone spacing and cone density were not calculated if we couldn't locate a first maximum of the radial profile. This occurred primarily for regions <0.15° retinal eccentricity arising from both the high cone density and from the rapid change in cone spacing with retinal eccentricity which resulted in blurring of the average cone images in this region.

Orientation of the local hexagon and local spacing anisotropy. For this analysis, for parafoveal data, we used the whole sliding window to locate and average cones. This served to increase the noise ratio in the average cone image and provide a better estimate of the local anisotropy. From the local averages we compute both the orientation and the local anisotropy of the regions in a series of steps (see Fig. 2):

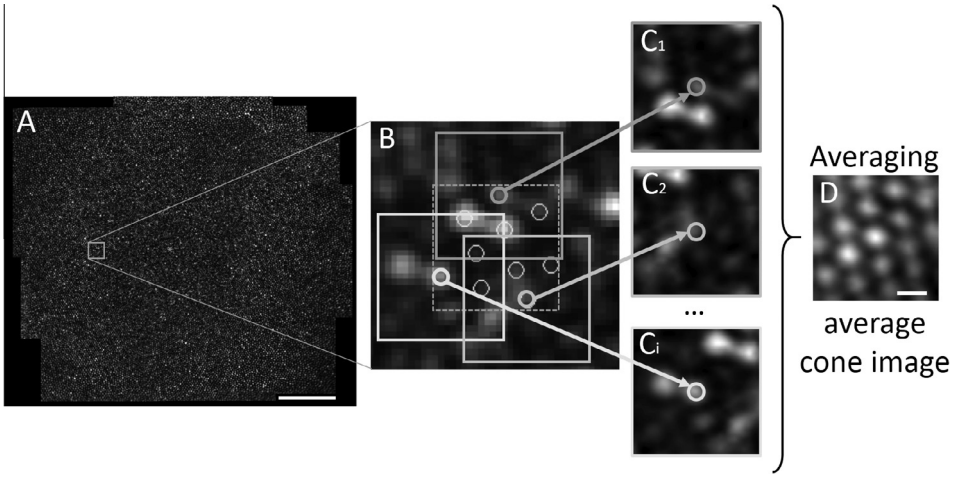

Fig. 1. Example of the calculation process for an average-cone image. (A) Foveal cone montage (from a 28yo female, with 0.5 μm/pixel sampling, scale bar represents 100 μm) and a sliding 50 × 50 pixel window (25 × 25 μm) at 0.43° nasally. (B) Example of the 50 × 50 pixel window selected for analysis where cones inside a centered 25 × 25 pixel (12.5 × 12.5 μm) region (centered dashed square) were automatically detected and ROI's of 25 × 25 pixels (12.5 × 12.5 μm) centered on the detected cones were extracted. The ROI's were rescaled after extraction (C1, C2 and Ci, examples of three ROI's (150 × 150 pixels, 12.5 × 12.5 μm)) and averaged, producing an average-cone image (D, scale bar represents 3 μm).

Please cite this article in press as: Sawides, L., et al. The organization of the cone photoreceptor mosaic measured in the living human retina. *Vision Research* (2016), http://dx.doi.org/10.1016/j.visres.2016.06.006

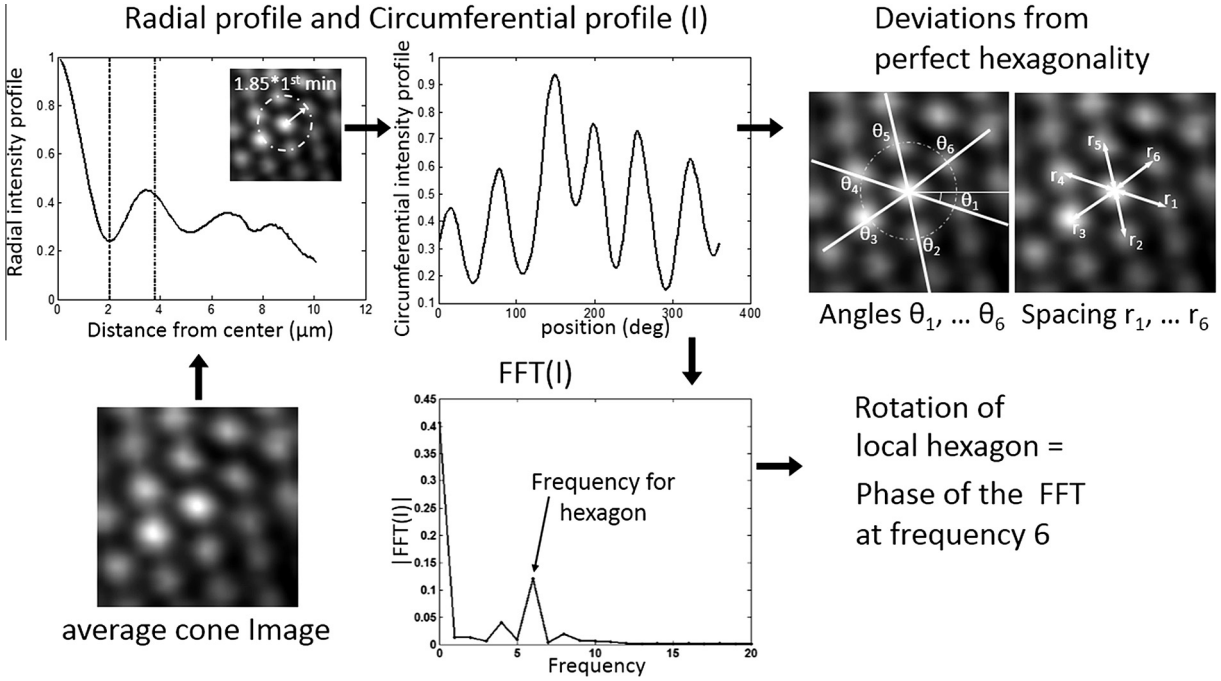

Fig. 2. Schematic of the analysis procedure applied to the average cone images (see Fig. 1). We first computed the radial intensity profile and then the circumferential intensity profile. From the circumferential profile, we used FFT to determine the degree of hexagonality and the rotation of the local hexagons, and the circumferential profile maxima to extract the angle of the principle axis (θ_1 to θ_6) and local spacing anisotropy (variation in distances, r1 to r6).

1. We first computed the radial intensity profile as described above. We then determined the minimum intensity along the radial profile, which in all cases generated a reliable minimum. From this minimum, we computed the circumferential Intensity profile (I) along a circle centered on the average cone and with a radius equal to 1.85× the distance to the minimum (Fig. 2, step 1). This factor of 1.85× corresponds to the coefficient by which we should multiply the first minimum found along the radial profile for an ideal hexagonal array of spheres, and thus for a perfect array would transect each surrounding cone. Additional spacing between cones, which occurs away from the fovea would cause this circle to fall short of the maximum, but still generates a radial profile with maximum near each surrounding cone. Similarly, local variations in spacing cause variations in the location of maxima in the circumferential intensity profile, and this variation is used in step 4 below.
2. We computed a Fast Fourier Transform (FFT) of the circumferential Intensity profile generated in step1. For a hexagonal array this generated a peak at a radial frequency of 6 (Fig. 2, step 2).
3. We estimated the signal to noise (S/N) ratio for each region as the ratio of the magnitude of the signal (FFT(6)) to the noise (the average of FFT(5) and FFT(7)) for hexagonal packing. For regions where the S/N ratio was less than 1, we tested for a peak in the FFT signal at frequencies corresponding to 4, 5, 7 or 8 neighbor regions, using the corresponding definition of S/N ratio. Regions where the S/N ratio was less than 1 were excluded from further processing as well as regions with alternative packing. The phase of the FFT(6) represents the average degree of rotation of the local hexagon and ranges from 0 to 60° (Fig. 2, step 3).
4. Deviations from perfect hexagonality (local anisotropies) were calculated by determining the angles (θ_1 to θ_6) from the positive horizontal through the central cone to the six maxima along the circumferential Intensity profile (I) and variations in the distance to the first maxima along these principle axes provide an estimate of the local spacing anisotropy, r1 to r6, of the local hexagon (Fig. 2, step 4).
5. Average spacing anisotropy. In order to determine the overall anisotropy for each region we combined the anisotropy across hexagons. We first calculated the normalized local spacing, e.g. $r_{i,norm} = \frac{r_i}{\left(\sum_1^6 r_i\right)/6}$ from all the average-cone images and excluded those values that were beyond the mean ± 2 SD of all the local hexagons of each subject. We then plotted the normalized local spacing as a function of angle θ_i (polar plot) considering all the local hexagons across subjects in 0.1° retinal eccentricity steps in the fovea and 0.5° retinal eccentricity step in the parafovea, getting one polar plot per retinal eccentricity on each meridian.

These polar plots were fitted to an ellipse where the ellipse orientation (orientation of the longest axis) and the ellipse eccentricity $\left(e = \sqrt{1 - \left(\frac{semiminor\ axis}{semimajor\ axis}\right)^2}\right)$ were calculated to estimate the local spacing anisotropy. An ellipse eccentricity e = 0 would represent a circle, with no predominant orientation.

Using this approach, we determined the local spacing anisotropy along the four primary meridians (Temporal, Nasal, Superior and Inferior). For the fovea we also determined the local spacing anisotropy along oblique meridians (SuperioTemporal, SuperioNasal, InferioTemporal and InferioNasal).

Sampling distribution and clustering. We measured the similarity of hexagon orientations across space to examine whether there was clustering of the sampling for the foveal cones that were within the central 1.4° × 1.4° of the retina. This resulted in 1089 25 × 25 pixel subregions for all subjects except S2 and S9, where 1058 and 1001 subregions were available respectively. Only regions that met the criteria for hexagonal packing (a peak for the nearest neighbor and a S/N ratio >1) were analyzed. Steps 1 to 3 of the analysis described above provided an estimate of the

Please cite this article in press as: Sawides, L., et al. The organization of the cone photoreceptor mosaic measured in the living human retina. *Vision Research* (2016), http://dx.doi.org/10.1016/j.visres.2016.06.006

average rotation of each average cone image, representing local hexagon orientation.

3. Results

3.1. Spatial variation in cone size and packing density

All subjects demonstrated the expected increase in cone spacing as retinal eccentricity increased. This change is visible in both the montage and in the average cone images as shown for one subject in Fig. 3 (subject S7, a 28 yo female). The average-cone images near the fovea (in the foveal montage) show a clear hexagonal packing while disarray increased with increasing retinal eccentricity.

3.2. Average cone spacing and cone density

As expected the average cone spacing varies significantly with both retinal eccentricity and meridian (ANOVA ($F(3,231) = 5.149$; $p = 0.0018$)) (Fig. 4) with the density being higher for the horizontal than vertical meridians at a fixed distance from the fovea. Fig. 4 shows that the current technique gives results essentially similar

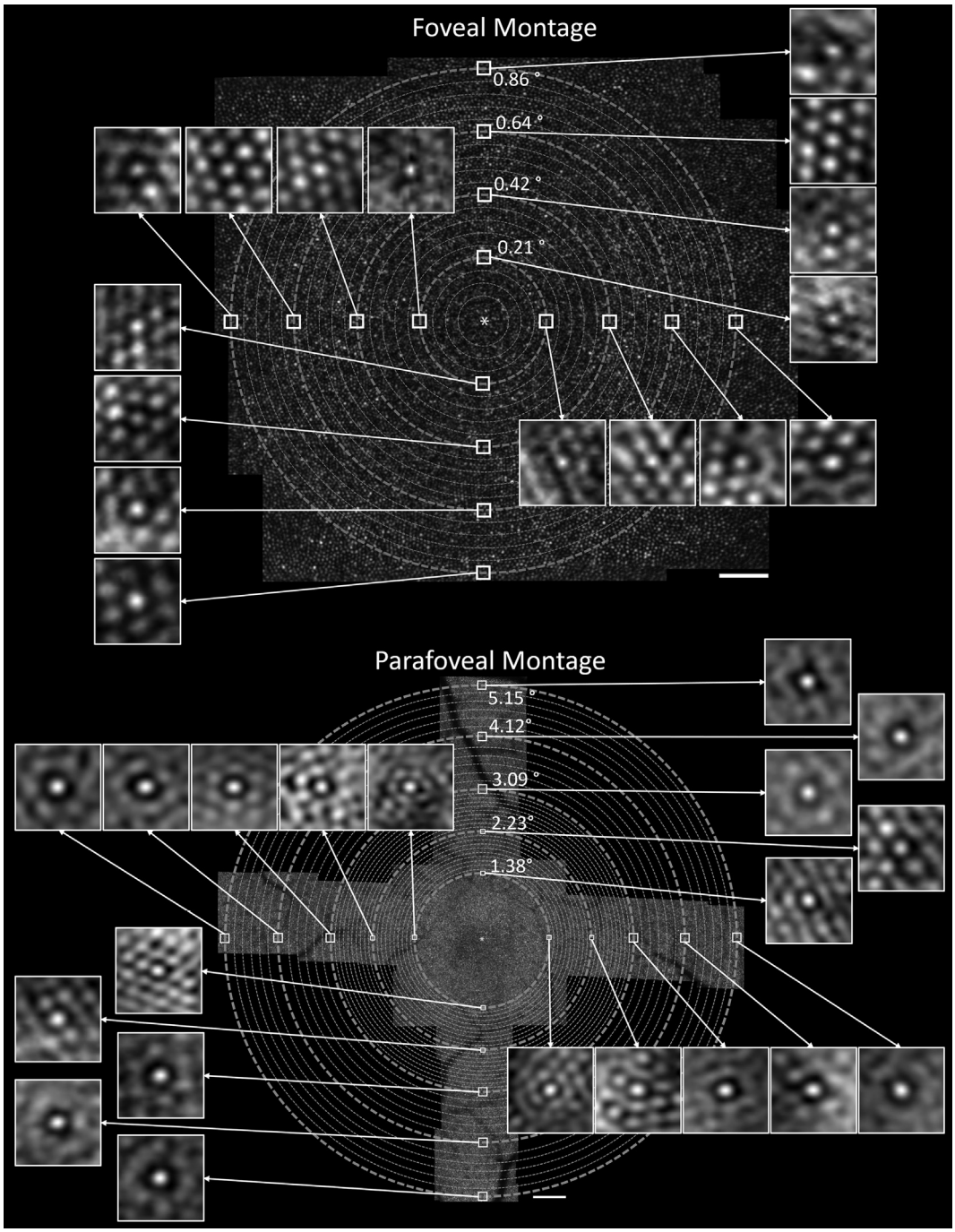

Fig. 3. Foveal (top) and parafoveal (bottom) montages for subject S7 (a 28 yo. Female). Scale bars represent 50 μm for foveal and 200 μm for parafoveal montages. Lines of isoeccentricity are drawn and average cone images are shown for selected locations along the four primary meridians. Average cone images are 12.5 × 12.5 μm for the foveal montage and 25 × 25 μm for the parafoveal montage.

Please cite this article in press as: Sawides, L., et al. The organization of the cone photoreceptor mosaic measured in the living human retina. *Vision Research* (2016), http://dx.doi.org/10.1016/j.visres.2016.06.006

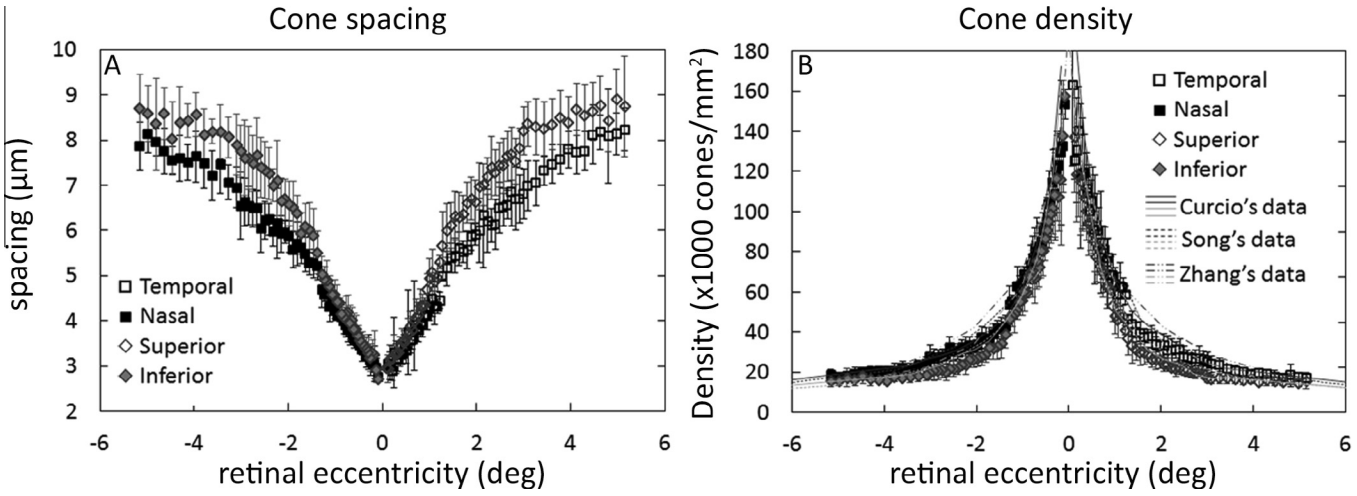

Fig. 4. Average cone spacing (panel A) and cone density (panel B) computed using the local cone average technique for the four primary meridians (Temporal, Nasal, Superior and Inferior). Error bars represent plus or minus one standard deviation across subjects.

to results from histological (Curcio et al., 1990) as well as AOSLO measurements (Song et al., 2011; Zhang et al., 2015).

3.3. Local spacing anisotropy

Across our entire data set, hexagonal packing was found in 89.6% of the regions studied according to our inclusion criteria (regions where the S/N ratio of the FFT(6) signal were less than 1 were excluded, as well as regions of alternative packing with 4n (3%), 5n (2.8%), 7n (0.5%) and 8n (0.4%) neighboring cones). There was also a significant local anisotropy in the cone spacing (Fig. 5). In Fig. 5 we plot line segments where the orientation represents the longest axis, and the length is proportional to the ellipse eccentricity (how different the length of the axes are) of the best fitting ellipse of the normalized local spacing, across subjects (one ellipse fitting for each retinal eccentricity on each meridian, in 0.1° retinal eccentricity steps in the fovea and 0.5° retinal eccentricity steps in the parafovea). In the fovea the cone spacing was larger along the horizontal than the vertical for all meridians (temporal, nasal, superior, inferior and oblique). Also, the orientation of the longer axis of the fitting ellipse is closer to 0° (3 ± 9° on average across meridians) in the fovea.

In the parafovea, the ellipse orientation (orientation of longest axis) is close to horizontal for the temporal and nasal meridians but reverses (the longer axis become more vertical) at about 2° retinal eccentricity for the superior meridian and 2.5° retinal eccentricity for the inferior meridian where the ellipse eccentricity also decreases. To analyze the significance of this pattern we performed ANOVAs showing a significant interaction of ellipse orientation vs meridian (ANOVA: $F(3,24) = 13.178$, $p < 0.0001$) and ellipse eccentricity vs meridian (ANOVA: $F(3,24) = 77.192$, $p < 0.0001$) for the parafoveal data but non-significant interactions between ellipse orientation or ellipse eccentricity vs meridian for the foveal data (ANOVA: $F(7,55) = 0.602$, $p = 0.751$ and ANOVA: $F(7,55) = 1.414$, $p = 0.2183$, respectively).

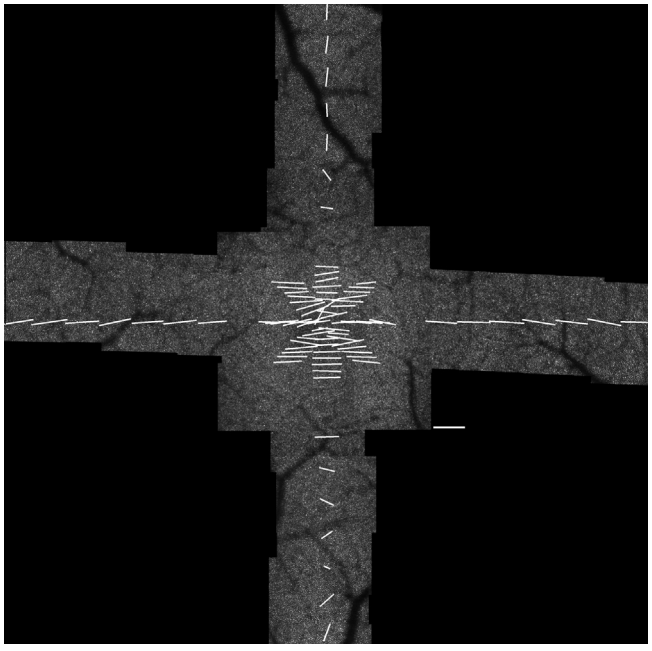

Fig. 5. Local axis of the best fitting ellipse of the normalized local spacing along the four primary meridians and for oblique meridians in the foveal region. For illustration purposes, we superimposed the average results across subjects on the parafoveal montage of S7. The white lines indicate the ellipse orientation (orientation of longest axis) and the magnitude of the ellipse eccentricity (length of white line). Scale bar represents an ellipse eccentricity of 0.5.

3.4. Sampling distribution and orientation clustering in the fovea

The orientation of local hexagons – assessed from the phase of the FFT(6) in each location – rotated from location to location (Fig. 6). Here the color scale rotates over 60° to capture the rotational symmetry of the hexagons. The angle of the local hexagons has an appearance of spatial coherence (like colors are near each other and the analysis of this spatial coherence is presented in the discussion).

4. Discussion

Adaptive optics imaging now allows us to systematically quantify the number of cones in the living human retina. The ability to quickly measure the sampling properties of the cone photoreceptor mosaic in a particular individual is allowing us to better understand differences in vision arising from cone sampling and how disease disrupts the photoreceptors. While counting every photoreceptor is the gold standard, and progress has been made towards improving the accuracy of automated algorithms (Chiu et al., 2013; Garrioch et al., 2012; Li & Roorda, 2007; Xue et al.,

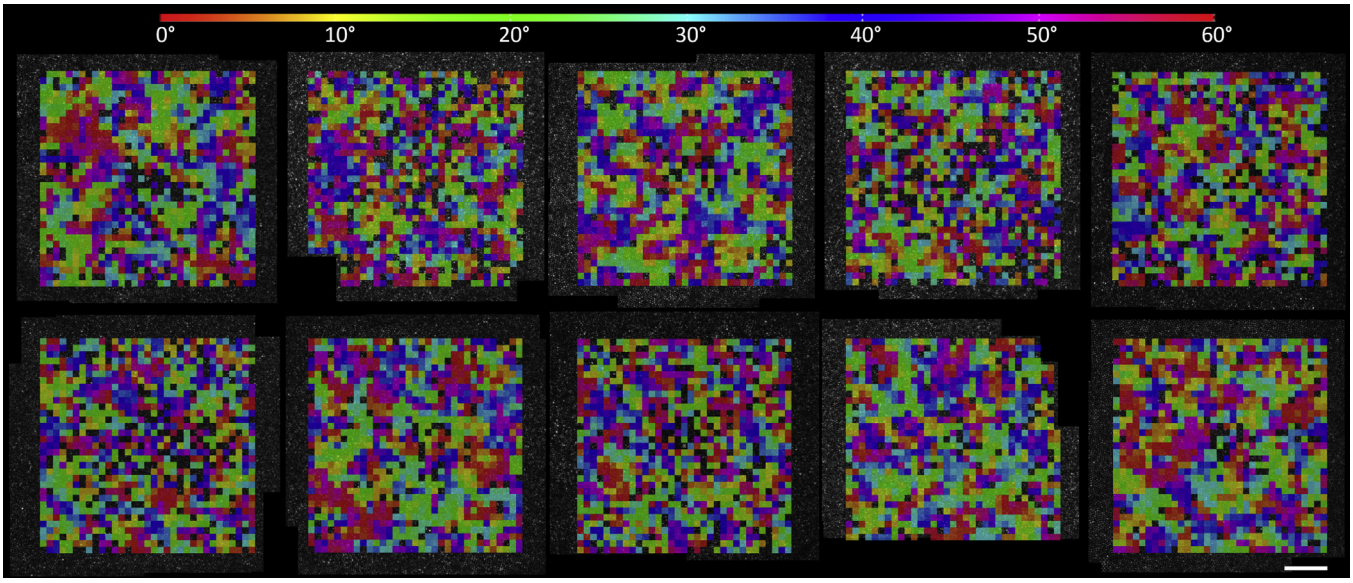

Fig. 6. Color-coded hexagon orientation maps for the 10 subjects. Scale bar represents 100 μm. For representation, each colored square (12.5 × 12.5 μm) corresponds to the orientation of local hexagon in this region. Regions that did not meet the criteria for hexagonal packing were left uncolored.

2007), it is nonetheless difficult, and techniques that provide averages, whether based on cross correlation (Li & Roorda, 2007; Rodieck, 1991), on the spatial frequency content (Cooper, Langlo, Dubra, & Carroll, 2013; Williams & Coletta, 1987; Yellott, 1982) or spatial arrangement (Mollon & Bowmaker, 1992; Roorda, Metha, Lennie, & Williams, 2001) are less sensitive to missing some of the cones. The technique we present is similar in concept, although it uses a shift and add approach rather than an auto-correlation approach. Our approach was able to capture the well-known first order spatial arrangement of the cones (spacing and packing density) using an automated detection algorithm where we decreased sensitivity such that it gave few false positives. Results with this algorithm were similar to those from techniques. Using our approach allows us to look at other features of cone photoreceptor packing in a more quantitative manner than has previously been achieved. While Voronoi analysis, which has been used extensively, allows some of these properties to be investigated, it is very sensitive to correctly identifying all the cones. The current method, while it has the disadvantage of being a local average, has the resulting advantage that it is accurate and less dependent on the identification of every cone in a region. Thus, we have been able to use it to look at both larger scale and smaller scale properties of cone mosaic organization.

4.1. Average cone spacing

The average-cone images near the fovea show a clear hexagonal packing while disorder increases with increasing retinal eccentricity, probably both because of decreased retinal coverage and intervening rods. Our finding of a difference in the density of packing with meridian is consistent with reports using other quantification techniques, which find that cones are more densely packed (higher cone density with a lower cone spacing) along the horizontal (Temporal, Nasal) meridians than along the vertical (Superior, Inferior) meridians using both histological samples (Curcio et al., 1990; Hirsch & Curcio, 1989) and *in vivo* imaging (Chui et al., 2008a, 2008b; Song et al., 2011; Zhang et al., 2015). In their recent study, Zhang et al. were able to estimate cone density at 0° retinal eccentricity, right in the center of the fovea and found higher density close to the fovea (<0.15° retinal eccentricity) by using optimized sampling windows of 5 × 5 um (for 0–0.3° retinal eccentricity), 10 × 10 μm for 0.5° retinal eccentricity and 40 × 40um (for 1–4° retinal eccentricity). Our use of a 12.5 × 12.5 um window is probably too large for these central cones, and thus led to less optimal average-cone images. For this reason we do not report cone spacing and cone density in the very center of the fovea using the cone-averaging method.

4.2. Local spacing anisotropy

As shown in Fig. 5, we found that local spacing of the average cones deviated from a pure hexagon. In general the individual regions had semi-hexagonal packing with the hexagon elongated in one direction, and typically with a greater spacing along the horizontal direction than along the vertical. For this reason we computed the average horizontal/vertical (ax/by) asymmetry from the data (Fig. 7) where we fitted one ellipse per retinal eccentricity (in 0.1° retinal eccentricity steps in the fovea and 0.5° retinal eccentricity steps in the parafovea) from the normalized local spacing across subjects. Here it is clear that cones are more widely spaced along the horizontal direction in the fovea (on average

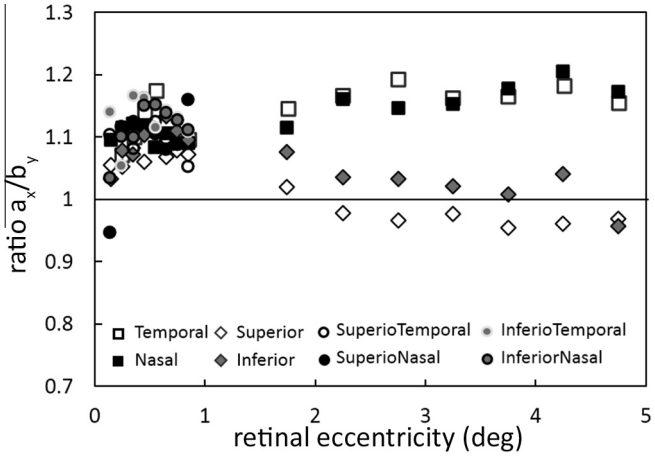

Fig. 7. Ratio a_x/b_y, (semi axis of the X and Y axis respectively of the non-tilted best fitting ellipse of the normalized local spacing) along the four primary meridians and for oblique meridians in the foveal region.

Please cite this article in press as: Sawides, L., et al. The organization of the cone photoreceptor mosaic measured in the living human retina. *Vision Research* (2016), http://dx.doi.org/10.1016/j.visres.2016.06.006

10 ± 3%). This local asymmetry is maintained for nasal and temporal meridians over the entire range we studied and increases in the parafovea (17 ± 2%). The change in orientation anisotropy in the superior and inferior meridian, that occurs at about 2° retinal eccentricity, is not due to a bias in the scanning imaging field while steering the beam along the meridians. This was tested by calibrating the scan with a high quality lens in place of the eye and a square ruled paper in the retinal conjugate plane. The measurements confirmed the ratio of horizontal and vertical sizes to be 1.0 while steering the beam in the four directions up to 5°. Distortion introduced while registering images during the montaging phase were also discarded as a source of this anisotropy by analyzing individual images at the different retinal location (before montaging) where we also found this change in tendency for the vertical meridians.

The existence of a spacing anisotropy is consistent with both psychophysical and histological measurements. Williams (1988) used the psychophysical identification of moiré zeros in interferometry, to measure cone spacing and found "a tendency for the spacing between cones to be slightly greater (14%) in a horizontal direction than a vertical direction at any retinal location" within 1.75° of the fovea and Coletta and Williams (1987) found that parafoveal cones on the nasal meridian are 7.4% more widely spaced horizontally. Results on the temporal and nasal meridians are also in agreement with histology data (Curcio & Sloan, 1992) where they found in one post-mortem human retina that "human cones are 10 to 15% farther apart in the radial direction than in the tangential direction (except at the edge of the rod-free zone)". For the superior and inferior meridians, however we do not find this radial orientation near the fovea but we do see it for larger retinal eccentricities (>2°). In the current study we did not collect data along the diagonals beyond approximately 1° so we can only confirm that beyond about 2° the data collected do show a tendency towards radial orientation for the major meridians. Our anisotropy results are also in agreement with previous data obtained with AOSLO imaging (Chui et al., 2008a, 2008b) and was consistent with the histological data found by Pum et al. (1990) with a mean vertical/horizontal compression factor of the mosaic to be 1/1.15. Thus on average all of the studies, including the current study seem to support this systematic local anisotropy with a larger cone spacing in the horizontal direction on the order of 10–15% of the average local cone spacing.

The local orientational anisotropy appears at first to contradict the result that average cone spacing decreases more rapidly with increasing retinal eccentricity along the vertical meridians, but it need not be in conflict. In order to pack cones in a manner that produces local hexagonal packing but also varies over space, the cone mosaic cannot be a perfect continuous hexagonal mosaic but must be either random or packed such that there are areas of similarly oriented local hexagons, but these differ in orientation from region to region as is seen in Fig. 6 and thus the global packing cannot be hexagonal and thus local packing does not directly predict global density.

4.3. Sampling distribution and determination of clustering in the fovea

We tested whether the impression of spatial coherence, where similar hexagon orientations are near each other (Fig. 6) was random. To do this we calculated the spatial extent and significance of orientation coherence by comparing the measured data to a random permutation of the subject's oriented local hexagons, which preserves the average orientation for each subject but alters the spatial coherence. For each orientation map, for each subject, we calculated the average difference in orientation from each hexagon and (1) its 4 adjacent neighbors (average distance of 14 μm), (2) its 4 diagonal neighbors (20 μm), (3) its 4 s-ring neighbors (28 μm) and (4) its 4 third-ring neighbors (42 μm). Fig. 8 shows an orientation map as well as its random permutation for subject S7, the change in degree of rotation of the hexagons from region to region for this subject for all the conditions (Fig. 8A) and the average change in degree of rotation as a function of the average distance from each hexagon, for each subject and on average (Fig. 8B) For the random permutation results, we show data for only the nearest neighbor analysis since all spatial combinations gave essentially identical results, as expected after random permutation. All first ring and second ring differences were significantly different from the random permutation (t-test $p < 0.05$), except in one subject (S4) where the first ring neighbor were different than random while the second ring neighbors were not. We conclude that cone orientations are clustered.

From the variation in orientation differences with distance (Fig. 8B) we estimated the size of these clusters. For distances greater than 40 μm there is no difference from the random permutation. This suggests that the cones are organized in patches, with orientation changes between patches, that can cover an area of approximately 24 μm radius (average distance between diagonal and second ring neighbors). This, due to the change of cone density over space in the fovea, would correspond to clusters of 35–243 cones within a patch in the central 1.4° (approximately 407 × 407 μm considering a conversion factor of 291 μm/°).

This result is consistent with histological measurements on post-mortem human retina. Pum et al. (1990) analyzed the cone mosaic in a foveal centered region of 218 × 158 μm by measuring individual cones and their neighbors without averaging. They found patches of oriented hexagonal packing (within ±5°internal axial orientation). These patches contained between 30 and 100 cones depending on the retinal eccentricity. They called this a "foveal iso-orientation areas", and these areas were separated by discrete discontinuities, "cracks" or "fracture zone, delineating lattice reorientations by 10–15 °" Wojtas, Wu, Ahnelt, Bones, and Millane (2008) used an automatic algorithm to process and analyze Differential Interference Contrast (DIC) microscopy images of the human fovea to study the orientation mapping of the cone mosaic. They found that with increasing retinal eccentricity, the hexagons tend to be elongated along the radial axis and found the mosaic partitioned in patches ("domains") of various sizes containing neighboring 6n cones, with a rotational shift from domain to domain of about 10°, with narrow regions containing neighboring 5n or 7n cones between them. These "fracture zone" included alternative packing of mainly 5 or 7 neighbor cones. Our current study also allows us to identify the alternative packings (region with 4n, 5n, 7n or 8n neighboring cones) but we did not see an obvious relation to the patches and we did not further analyze these regions since they are relatively infrequent in this data set.

While some authors have associated the interruptions of the regular foveal matrix with the presence of short-wave cones (Ahnelt et al., 1987; Hofer, Carroll, Neitz, Neitz, & Williams, 2005), or individual cone class submosaics, it is unlikely that the spatial organization of the orientated regions we measured in the fovea are related to the spatial organization of the long-(L), middle-(M) and short-(S) wavelength sensitive submosaics. Histological studies (Curcio et al., 1991) and adaptive optics based imaging (Hofer et al., 2005; Roorda & Williams, 1999; Roorda et al., 2001) have shown that S-cones are irregularly spaced, randomly distributed and missing from the central 0.35° in the fovea centralis and similarly the L and M cone submosaics are found to be randomly interleaved within the full cone mosaic studied in primates and human eyes (Bowmaker, Parry, & Mollon, 2003; Gowdy & Cicerone, 1998; Mollon & Bowmaker, 1992). Moreover, there are large individual differences in the relative numerosity of L and M cones (Roorda & Williams, 1999; Rushton & Baker, 1964) but our results show relatively similar orientation coherence across all 10 subjects.

Please cite this article in press as: Sawides, L., et al. The organization of the cone photoreceptor mosaic measured in the living human retina. *Vision Research* (2016), http://dx.doi.org/10.1016/j.visres.2016.06.006

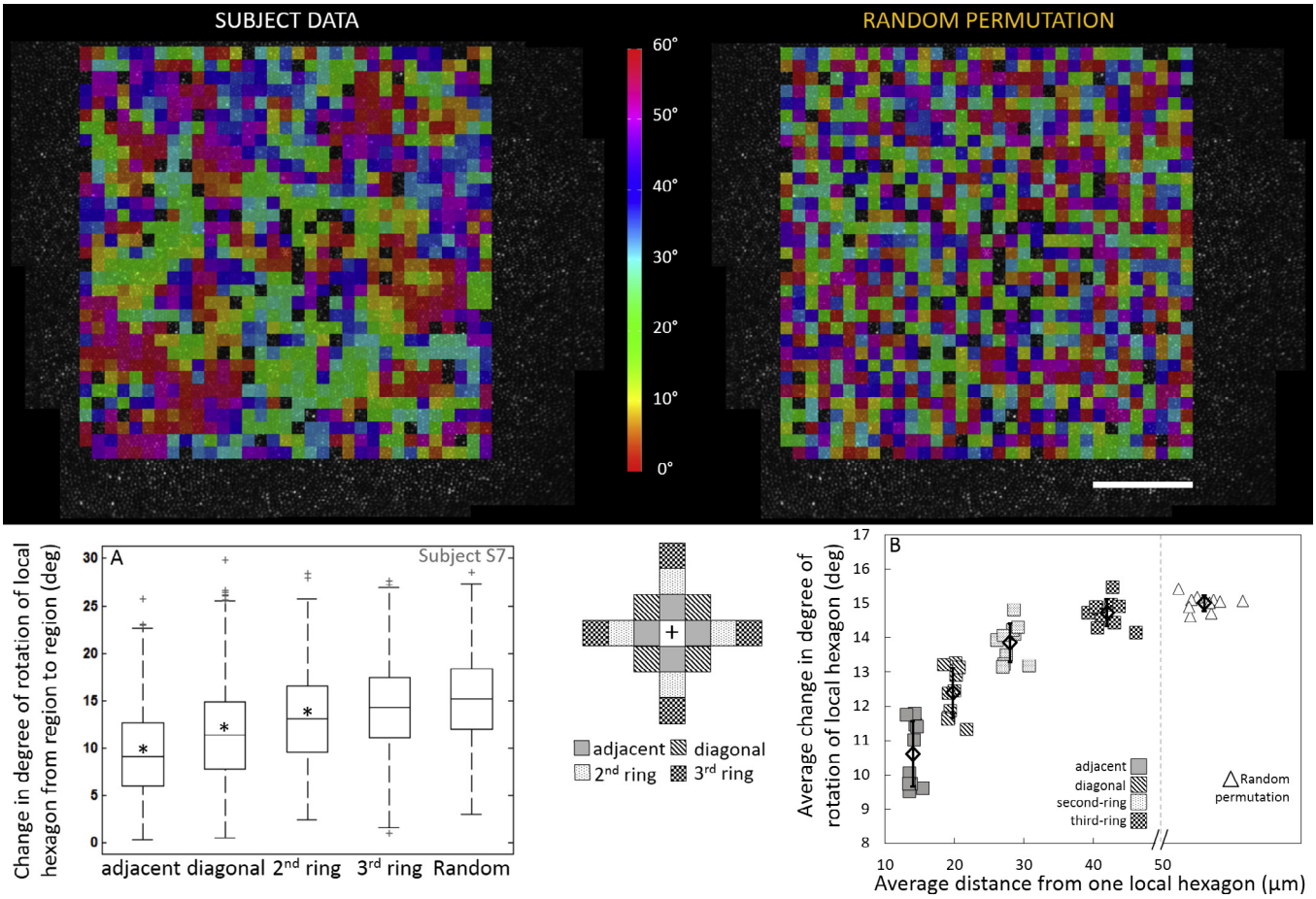

Fig. 8. Top row: Foveal montage (S7, 28yo female, scale bar represents 100 μm) with color-coded orientation map, random permutation of the oriented local hexagons. Bottom row: (middle) examples of one local hexagon (+) and its 4 adjacent, 4 diagonal, 4 s-ring and 4 third-ring neighbors. (A) Change in degree of rotation of each hexagon from region to region for subject S7 (* stands for a statistically significantly difference from random) and (B) average degree of rotation change as a function of average distance.

4.4. Potential uses of this technique

While we have used this average cone approach to analyze the normal retina of 10 subjects, it may be of use in clinical studies as well. Baraas et al. (2007) demonstrated with a Voronoi analysis that tritanopes – who suffer from an inherited autosomal dominant abnormality of short-wavelength-sensitive- (S-) cone function- shows only 55% of 6-sided polygons against 70% for normal. Pum et al. (1990) found that "The foveal mosaic from a glaucomatous eye reveals severe lattice degradation throughout the rod-free zone, presumably due to extensive receptor loss". Because of the simplicity of our approach, and the fact that it is relatively robust to algorithmically missing some of the cones, it may be a reasonable alternative to Voronoi analysis, and could easily be adjusted to also provide estimates of the nature of the mosaic in non-hexagonal regions from the peak of the FFT analysis as well as to provide other estimates of spatial coherence by examining the width of the cone averages at increasing distances from the center. The finding on the spatial variations in hexagonal packing and how cones are organized in the fovea may also have a significant impact when modeling the eye (Ahumada & Poirson, 1987; Springer & Hendrickson, 2004, 2005) and the development of the foveal cones in parallel with the development of the retinal vasculature (Diaz-Araya & Provis, 1992; Hendrickson, Possin, Vajzovic, & Toth, 2012; Hendrickson & Yuodelis, 1984; Provis, Dubis, Maddess, & Carroll, 2013; Springer, 1999; Yuodelis & Hendrickson, 1986) as pointed out by Ahnelt (1998) neighboring 5n or 7n foveal cones "are arranged in linear series subdividing the mosaic into patches with similar crystalline orientation, possibly reorganizing and relaxing the lattice from shearing stress accumulating during inward migration and condensation". A potential disadvantage of our technique is that we typically average over at least 5–10 cones in order to get a robust FFT output in all subjects at almost all locations from a given imaging session. This averaging process necessarily smooths out some of the fine spatial detail.

5. Conclusion

We have implemented and applied a method that allows rapid automated estimates of cone packing properties and provides an analysis of individual difference in cone spacing and local anisotropies of the hexagonal cone array. This data provides insight into the organization of the in-vivo cone photoreceptors mosaic, as it is, to our knowledge the first analysis of the *in vivo* patchwise organization of the foveal cone photoreceptors, with areas of consistent organization extending across hundreds cones. This technique will allow further investigations of the normal cone mosaic as well as disease-induced changes in the cone packing.

Disclosure statement

The authors declare that they have no conflict of interest.

Please cite this article in press as: Sawides, L., et al. The organization of the cone photoreceptor mosaic measured in the living human retina. *Vision Research* (2016), http://dx.doi.org/10.1016/j.visres.2016.06.006

Acknowledgments

This work was funded by Foundation Fighting Blindness grant TA-CL-0613-0617-IND, NEI EY004395, "Investigations of Human Cone Photoreceptor Alignment" and NEI P30 EY019008-01A1 "Core Grant for Vision Science at Indiana University".

References

Ahnelt, P. K. (1998). The photoreceptor mosaic. *Eye (Lond), 12*(Pt 3b), 531–540.
Ahnelt, P. K., Kolb, H., & Pflug, R. (1987). Identification of a subtype of cone photoreceptor, likely to be blue sensitive, in the human retina. *Journal of Comparative Neurology, 255*(1), 18–34.
Ahumada, A. J., Jr., & Poirson, A. (1987). Cone sampling array models. *Journal of the Optical Society of America A: Optics, Image Science, and Vision, 4*(8), 1493–1502.
Baraas, R. C., Carroll, J., Gunther, K. L., Chung, M., Williams, D. R., Foster, D. H., et al. (2007). Adaptive optics retinal imaging reveals S-cone dystrophy in tritan color-vision deficiency. *Journal of the Optical Society of America A: Optics, Image Science, and Vision, 24*(5), 1438–1447.
Bowmaker, J., Parry, J., & Mollon, J. (2003). The arrangement of L and M cones in human and a primate retina. *Normal and Defective Colour Vision*, 39–50.
Burns, S. A., Elsner, A. E., Chui, T. Y., Vannasdale, J., Dean, A., Clark, C. A., ... Phan, A.-D. T. (2014). In vivo adaptive optics microvascular imaging in diabetic patients without clinically severe diabetic retinopathy. *Biomedical Optics Express, 5*(3), 961–974.
Burns, S. A., Zou, W., Qi, X., Zhong, Z., & Huang, G. (2011). Rapid cone AOSLO imaging and analysis. *Investigative Ophthalmology & Visual Science, 52*(14). 3195–3195.
Carroll, J., Baraas, R. C., Wagner-Schuman, M., Rha, J., Siebe, C. A., Sloan, C., ... Neitz, M. (2009). Cone photoreceptor mosaic disruption associated with Cys203Arg mutation in the M-cone opsin. *Proceedings of the National Academy of Sciences of the United States of America, 106*(49), 20948–20953.
Chiu, S. J., Lokhnygina, Y., Dubis, A. M., Dubra, A., Carroll, J., Izatt, J. A., et al. (2013). Automatic cone photoreceptor segmentation using graph theory and dynamic programming. *Biomedical Optics Express, 4*(6), 924–937.
Choi, S. S., Doble, N., Hardy, J. L., Jones, S. M., Keltner, J. L., Olivier, S. S., et al. (2006). In vivo imaging of the photoreceptor mosaic in retinal dystrophies and correlations with visual function. *Investigative Ophthalmology & Visual Science, 47*(5), 2080–2092.
Chui, T. Y., Song, H., & Burns, S. A. (2008a). Adaptive-optics imaging of human cone photoreceptor distribution. *Journal of the Optical Society of America A: Optics, Image Science, and Vision, 25*(12), 3021–3029.
Chui, T. Y., Song, H., & Burns, S. A. (2008b). Individual variations in human cone photoreceptor packing density: Variations with refractive error. *Investigative Ophthalmology & Visual Science, 49*(10), 4679–4687.
Coletta, N. J., & Williams, D. R. (1987). Psychophysical estimate of extrafoveal cone spacing. *Journal of the Optical Society of America A: Optics, Image Science, and Vision, 4*(8), 1503–1513.
Cooper, R. F., Langlo, C. S., Dubra, A., & Carroll, J. (2013). Automatic detection of modal spacing (Yellott's ring) in adaptive optics scanning light ophthalmoscope images. *Ophthalmic and Physiological Optics, 33*(4), 540–549.
Curcio, C. A., Allen, K. A., Sloan, K. R., Lerea, C. L., Hurley, J. B., Klock, I. B., et al. (1991). Distribution and morphology of human cone photoreceptors stained with anti-blue opsin. *Journal of Comparative Neurology, 312*(4), 610–624.
Curcio, C. A., & Sloan, K. R. (1992). Packing geometry of human cone photoreceptors: Variation with eccentricity and evidence for local anisotropy. *Visual Neuroscience, 9*(2), 169–180.
Curcio, C. A., Sloan, K. R., Kalina, R. E., & Hendrickson, A. E. (1990). Human photoreceptor topography. *Journal of Comparative Neurology, 292*(4), 497–523.
Dees, E. W., Dubra, A., & Baraas, R. C. (2011). Variability in parafoveal cone mosaic in normal trichromatic individuals. *Biomedical Optics Express, 2*(5), 1351–1358.
Diaz-Araya, C., & Provis, J. M. (1992). Evidence of photoreceptor migration during early foveal development: A quantitative analysis of human fetal retinae. *Visual Neuroscience, 8*(6), 505–514.
Ferguson, R. D., Zhong, Z., Hammer, D. X., Mujat, M., Patel, A. H., Deng, C., ... Burns, S. A. (2010). Adaptive optics scanning laser ophthalmoscope with integrated wide-field retinal imaging and tracking. *Journal of the Optical Society of America A: Optics, Image Science, and Vision, 27*(11), A265–A277.
Garrioch, R., Langlo, C., Dubis, A. M., Cooper, R. F., Dubra, A., & Carroll, J. (2012). Repeatability of in vivo parafoveal cone density and spacing measurements. *Optometry and Vision Science, 89*(5), 632–643.
Gowdy, P. D., & Cicerone, C. M. (1998). The spatial arrangement of the L and M cones in the central fovea of the living human eye. *Vision Research, 38*(17), 2575–2589.
Hendrickson, A., Possin, D., Vajzovic, L., & Toth, C. A. (2012). Histologic development of the human fovea from midgestation to maturity. *American Journal of Ophthalmology, 154*(5). 767–778.e2.
Hendrickson, A. E., & Yuodelis, C. (1984). The morphological development of the human fovea. *Ophthalmology, 91*(6), 603–612.
Hirsch, J., & Curcio, C. A. (1989). The spatial resolution capacity of human foveal retina. *Vision Research, 29*(9), 1095–1101.
Hofer, H., Carroll, J., Neitz, J., Neitz, M., & Williams, D. R. (2005). Organization of the human trichromatic cone mosaic. *Journal of Neuroscience, 25*(42), 9669–9679.
Huang, G., Zhong, Z., Zou, W., & Burns, S. A. (2011). Lucky averaging: Quality improvement of adaptive optics scanning laser ophthalmoscope images. *Optics Letters, 36*(19), 3786–3788.
Li, K. Y., & Roorda, A. (2007). Automated identification of cone photoreceptors in adaptive optics retinal images. *Journal of the Optical Society of America A: Optics, Image Science, and Vision, 24*(5), 1358–1363.
Li, K. Y., Tiruveedhula, P., & Roorda, A. (2010). Intersubject variability of foveal cone photoreceptor density in relation to eye length. *Investigative Ophthalmology & Visual Science, 51*(12), 6858–6867.
Liang, J., Williams, D. R., & Miller, D. T. (1997). Supernormal vision and high-resolution retinal imaging through adaptive optics. *Journal of the Optical Society of America A: Optics, Image Science, and Vision, 14*(11), 2884–2892.
Lombardo, M., Lombardo, G., Schiano Lomoriello, D., Ducoli, P., Stirpe, M., & Serrao, S. (2013). Interocular symmetry of parafoveal photoreceptor cone density distribution. *Retina, 33*(8), 1640–1649.
Lombardo, M., Serrao, S., Ducoli, P., & Lombardo, G. (2013). Eccentricity dependent changes of density, spacing and packing arrangement of parafoveal cones. *Ophthalmic and Physiological Optics, 33*(4), 516–526.
Loquin, K., Bloch, I., Nakashima, K., Rossant, F., Boelle, P.-Y., & Paques, M. (2012). Automatic photoreceptor detection in in-vivo adaptive optics retinal images: Statistical validation. In *Image analysis and recognition* (pp. 408–415). Springer.
Marcos, S., & Burns, S. A. (1999). Cone spacing and waveguide properties from cone directionality measurements. *Journal of the Optical Society of America A: Optics, Image Science, and Vision, 16*(5), 995–1004.
Marcos, S., Navarro, R., & Artal, P. (1996). Coherent imaging of the cone mosaic in the living human eye. *Journal of the Optical Society of America A: Optics, Image Science, and Vision, 13*(5), 897–905.
Marcos, S., Tornow, R. P., Elsner, A. E., & Navarro, R. (1997). Foveal cone spacing and cone photopigment density difference: Objective measurements in the same subjects. *Vision Research, 37*(14), 1909–1915.
Merino, D., Duncan, J. L., Tiruveedhula, P., & Roorda, A. (2011). Observation of cone and rod photoreceptors in normal subjects and patients using a new generation adaptive optics scanning laser ophthalmoscope. *Biomedical Optics Express, 2*(8), 2189–2201.
Mollon, J. D., & Bowmaker, J. K. (1992). The spatial arrangement of cones in the primate fovea. *Nature, 360*(6405), 677–679.
Osterberg, G. (1935). Topography of the layer of rod and cones in the human retina. *Acta Ophthalmologica, 13*(Suppl 6(1)), 103.
Park, S. P., Chung, J. K., Greenstein, V., Tsang, S. H., & Chang, S. (2013). A study of factors affecting the human cone photoreceptor density measured by adaptive optics scanning laser ophthalmoscope. *Experimental Eye Research, 108*, 1–9.
Provis, J. M., Dubis, A. M., Maddess, T., & Carroll, J. (2013). Adaptation of the central retina for high acuity vision: Cones, the fovea and the avascular zone. *Prog Retin Eye Res, 35*, 63–81.
Pum, D., Ahnelt, P. K., & Grasl, M. (1990). Iso-orientation areas in the foveal cone mosaic. *Visual Neuroscience, 5*(6), 511–523.
Rodieck, R. W. (1991). The density recovery profile: A method for the analysis of points in the plane applicable to retinal studies. *Visual Neuroscience, 6*(2), 95–111.
Roorda, A., Metha, A. B., Lennie, P., & Williams, D. R. (2001). Packing arrangement of the three cone classes in primate retina. *Vision Research, 41*(10–11), 1291–1306.
Roorda, A., Romero-Borja, F., Donnelly Iii, W., Queener, H., Hebert, T., & Campbell, M. (2002). Adaptive optics scanning laser ophthalmoscopy. *Optics Express, 10*(9), 405–412.
Roorda, A., & Williams, D. R. (1999). The arrangement of the three cone classes in the living human eye. *Nature, 397*(6719), 520–522.
Rossi, E. A., & Roorda, A. (2010). The relationship between visual resolution and cone spacing in the human fovea. *Nature Neuroscience, 13*(2), 156–157.
Rushton, W. A., & Baker, H. D. (1964). Red/green sensitivity in normal vision. *Vision Research, 4*(1), 75–85.
Shapiro, M., Schein, S., & De Monasterio, F. (1985). Regularity and structure of the spatial pattern of blue cones of macaque retina. *Journal of the American Statistical Association, 80*(392), 803–812.
Song, H., Chui, T. Y. P., Zhong, Z., Elsner, A. E., & Burns, S. A. (2011). Variation of cone photoreceptor packing density with retinal eccentricity and age. *Investigative Ophthalmology & Visual Science, 52*(10), 7376–7384.
Springer, A. D. (1999). New role for the primate fovea: A retinal excavation determines photoreceptor deployment and shape. *Visual Neuroscience, 16*(4), 629–636.
Springer, A. D., & Hendrickson, A. E. (2004). Development of the primate area of high acuity. 1. Use of finite element analysis models to identify mechanical variables affecting pit formation. *Visual Neuroscience, 21*(1), 53–62.
Springer, A. D., & Hendrickson, A. E. (2005). Development of the primate area of high acuity, 3: Temporal relationships between pit formation, retinal elongation and cone packing. *Visual Neuroscience, 22*(2), 171–185.
Williams, D. R. (1988). Topography of the foveal cone mosaic in the living human eye. *Vision Research, 28*(3), 433–454.
Williams, D. R., & Coletta, N. J. (1987). Cone spacing and the visual resolution limit. *Journal of the Optical Society of America A: Optics, Image Science, and Vision, 4*(8), 1514–1523.
Wojtas, D. H., Wu, B., Ahnelt, P. K., Bones, P. J., & Millane, R. P. (2008). Automated analysis of differential interference contrast microscopy images of the foveal cone mosaic. *Journal of the Optical Society of America A: Optics, Image Science, and Vision, 25*(5), 1181–1189.
Xue, B., Choi, S. S., Doble, N., & Werner, J. S. (2007). Photoreceptor counting and montaging of en-face retinal images from an adaptive optics fundus camera.

Please cite this article in press as: Sawides, L., et al. The organization of the cone photoreceptor mosaic measured in the living human retina. *Vision Research* (2016), http://dx.doi.org/10.1016/j.visres.2016.06.006

Journal of the Optical Society of America A: Optics, Image Science, and Vision, 24(5), 1364–1372.

Yellott, J. Jr., (1982). Spectral analysis of spatial sampling by photoreceptors: Topological disorder prevents aliasing. *Vision Research, 22*(9), 1205–1210.

Yuodelis, C., & Hendrickson, A. (1986). A qualitative and quantitative analysis of the human fovea during development. *Vision Research, 26*(6), 847–855.

Zhang, T., Godara, P., Blanco, E. R., Griffin, R. L., Wang, X., Curcio, C. A., et al. (2015). Variability in human cone topography assessed by adaptive optics scanning laser ophthalmoscopy. *American Journal of Ophthalmology*.

Zou, W., Qi, X., & Burns, S. A. (2008). Wavefront-aberration sorting and correction for a dual-deformable-mirror adaptive-optics system. *Optics Letters, 33*(22), 2602–2604.

Please cite this article in press as: Sawides, L., et al. The organization of the cone photoreceptor mosaic measured in the living human retina. *Vision Research* (2016), http://dx.doi.org/10.1016/j.visres.2016.06.006